

Structural and electronic origin of the magnetic structures in hexagonal LuFeO₃

Hongwei Wang^{1,2}, Igor V. Solovyev³, Wenbin Wang⁴, Xiao Wang⁵, Philip J. Ryan⁶, David J. Keavney⁶, Jong-Woo Kim⁶, Thomas Z. Ward⁷, Leyi Zhu⁸, Jian Shen⁴, X. M. Cheng⁵, Lixin He², Xiaoshan Xu^{5,7,9,*}, and Xifan Wu^{2,*}

¹*Department of Physics, Temple University, Philadelphia, Pennsylvania 19122, USA*

²*Key Laboratory of Quantum Information, University of Science and Technology of China, Hefei, Anhui, 230026, People's Republic of China*

³*Computational Materials Science Unit, National Institute for Materials Science, 1-2-1 Sengen, Tsukuba 305-0047, Japan*

⁴*Department of Physics, Fudan University, Shanghai 200433, China*

⁵*Department of Physics, Bryn Mawr College, Bryn Mawr, PA 19010, USA*

⁶*Advanced Photon Source, Argonne National Laboratory, Argonne, IL 60439, USA*

⁷*Materials Science and Technology Division, Oak Ridge National Laboratory, Oak Ridge, TN 37831, USA*

⁸*Materials Science Division, Argonne National Laboratory, Argonne, IL 60439, USA and*

⁹*Department of Physics and Astronomy, University of Nebraska-Lincoln, NE 68588, USA*

Using combined theoretical and experimental approaches, we studied the structural and electronic origin of the magnetic structure in hexagonal LuFeO₃. Besides showing the strong exchange coupling that is consistent with the high magnetic ordering temperature, the previously observed spin reorientation transition is explained by the theoretically calculated magnetic phase diagram. The structural origin of this spin reorientation that is responsible for the appearance of spontaneous magnetization, is identified by theory and verified by x-ray diffraction and absorption experiments.

PACS numbers: 77.80.-e, 63.20.dk, 77.55.Nv, 61.05.cp, 75.25.-j

I. INTRODUCTION

While the ferroelectricity in materials is naturally connected to structural distortions that breaks the spatial inversion symmetry^{1,2}, the relation between spontaneous magnetization and structure is not obvious because no spatial symmetry is broken by ferromagnetism (FM). Nevertheless, magnetic orderings in a material are tied to the structure, and the ties are particularly important in multiferroic materials³ in which structural distortions may mediate couplings between ferroelectricity and ferromagnetism or even generate ferroelectric ferromagnets which are extremely rare⁴.

The recently discovered room temperature multiferroic, i.e. hexagonal LuFeO₃ (hLFO)⁵, provides an rare case multiferroic material in which spontaneous electric and magnetic polarizations coexist. On one hand, ferroelectricity appears below $T_C=1050$ K resulting from a $P6_3/mmc \rightarrow P6_3cm$ structure distortion, which can be decomposed in terms of three phonon modes (Fig. 1(a))^{5,6}. On the other hand, spin frustration in hLFO presents rich magnetic phases⁷. Intriguingly, below the Néel temperature $T_N = 440$ K, magnetic order in hLFO transits again from B_2 to A_2 (Fig. 1(b)) at $T_R=130$ K⁵ by a spin reorientation (SR), resulting in a weak ferromagnetism due to the Dzyaloshinskii-Moriya and single-ion anisotropy mechanism⁸⁻¹². Similar to hexagonal YMnO₃, the K_3 phonon is believed to be the driving force that induces the instability of Γ_2^- that is responsible for the ferroelectricity¹³⁻¹⁵. However, the origin of the SR is still elusive. Since the SR is the direct cause of spontaneous magnetization, elucidating the origin may provide a way to effectively tune T_R , or even a novel route for realizing a coexistence of spontaneous electric and magnetic polarizations above room temper-

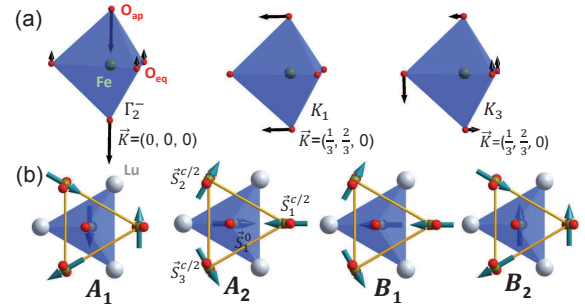


FIG. 1: (Color online.) (a) Displacement patterns of the FeO₅ local environment (trigonal bipyramid) in the three phonon modes that freeze in the $P6_3/mmc \rightarrow P6_3cm$ structural transition in hexagonal ferrites (h-RFeO₃). The arrows indicate the relative displacement of the atoms. \vec{K} is the wave vector of the modes in the reciprocal space of the $P6_3/mmc$ structure. (b) Four independent spin structures (A_1 , A_2 , B_1 , and B_2) of the 120-degree magnetic orders viewed along the c axis. The arrows indicate the spins ($\vec{S}_i^{Z_{Fe}}$) on the Fe sites. The Fe sites shown in the polyhedra are in the $Z_{Fe} = 0$ layer while all the other Fe sites are in the $Z_{Fe} = c/2$ layers. In the B (A) phase, \vec{S}_1^0 is parallel (antiparallel) to $\vec{S}_1^{c/2}$.

ature¹⁶⁻¹⁸.

Previous studies in hexagonal manganites (h-RMO, isomorphic to hLFO) indicate rich magnetic phases due to the SR that is strongly coupled to the crystal structure^{3,19,20}. However, the multiple degrees of freedom involved (spin and orbital degrees of freedom of the electrons and the lattice) complicate the problem in h-RMO²¹. The complexity may be reduced in h-LFO, in which Fe³⁺ can be considered a spin-only ion with nearly spherical $3d^5$ electronic configuration. Therefore, a better understanding on the SR in hLFO is possible, particularly in terms

of the phonon modes (Fig. 1(b)); it may also be an important step in understanding the more complex SR in h-RMO²¹, in which the single-ion anisotropy is expected to play a more important role.

To address the above issues, we perform combined theoretical and experimental studies of the exchange interactions and its couplings to the structural instabilities in hLFO. We apply an extended Kugel-Khomskii (KK) model for superexchange (SE) interactions²² based on localized Wannier functions (LWFs)^{23,24}. While the antiferromagnetic (AFM) exchange coupling is dominated by the intralayer superexchange, the model clearly shows that the singly occupied d_{z^2} orbital in hLFO greatly increases the exchange coupling compared with the empty d_{z^2} in LuMnO₃ (LMO). The interlayer exchange, although much weaker in magnitude, is key to the SR. Our first-principles calculations show that SR is strongly coupled to the K_1 phonon mode and only weakly dependent on K_3 mode. Our theory indicates that the atomic displacements of K_1 mode is responsible for the SR. This scenario is then confirmed by our x-ray diffraction and x-ray absorption experiments.

II. COMPUTATIONAL METHODS AND EXPERIMENTAL TECHNIQUES

Our extended KK model^{22,27} is built on the basis of LWFs generated from density functional theory (DFT) calculations. The screened Coulomb interactions between LWFs are computed in the constrained random-phase approximation²⁵⁻²⁷. The calculations of spin phonon coupling is performed within DFT+U scheme^{27,28}. We have adopted the four-state method²⁹ in computing the exchange coupling strengths. hLFO films (50 nm thick) were grown on Al₂O₃ (0001) substrates with and without a (30 nm) Pt buffer layer using pulsed laser deposition. The x-ray diffraction (XRD) and x-ray absorption spectroscopy (XAS) measurements were carried out in 6-ID-B beam line on the h-LuFeO₃/Al₂O₃ film and in 4-ID-C beam line on the h-LuFeO₃/Pt/Al₂O₃ film respectively at the Advanced Photon Source at various temperature.

III. RESULTS AND DISCUSSION

In hexagonal ferrites, the exchange interaction between the Fe sites can be written as

$$H_{ex} = H_{ex}^{a-b} + H_{ex}^c \quad (1)$$

where H_{ex}^{a-b} is the intra-layer exchange interaction and H_{ex}^c is the inter-layer exchange interaction considering only the nearest neighbors.

As shown in Fig. 2, the intra-layer SE interaction $H_{ex}^{a-b} = \sum_{i,j,Z_{Fe}} \mathcal{J}_{i,j}^{a-b} \vec{S}_i^{Z_{Fe}} \cdot \vec{S}_j^{Z_{Fe}}$ between two nearest neighbor (NN) Fe atoms at site i and j are mediated

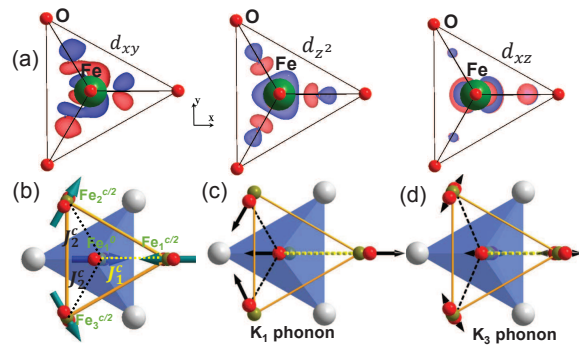


FIG. 2: (Color online.) (a) Representative d_{xy} , d_{z^2} , and d_{xz} -like LWFs viewed from [001] direction. (b) illustrations of two independent SSE paths J_1^c and J_2^c between Fe₀ at $z/c = 0$ and three neighboring iron ions Fe₁, Fe₂, and Fe₃ at $z/c = 1/2$ (c) atomic displacements of K_1 phonon mode, (d) atomic displacements of K_3 phonon mode, viewed from [001] direction.

by corner sharing oxygen atoms. In order to elucidate the electronic structural origin, we employ the extended KK model and the SE coupling can be expressed as

$$\mathcal{J}_{i,j}^{a-b} = \sum_{\alpha,\alpha'} J_{\alpha,\alpha'}^{AFM} + \sum_{\alpha,\beta} J_{\alpha,\beta}^{FM} \quad (2)$$

The first term in Eq. (2) describes the AFM-type coupling resulting from virtual hopping processes between two half-filled d bands; while the second term depicts the competing FM-type coupling from hoppings from half-filled d orbital (α) to empty ones (β)²⁷. The computed individual exchange interaction as well as the overall SE coupling J_{MOD}^{a-b} for both hLFO and hLMO are presented in Table I. The total exchange coupling J_{DFT}^{a-b} from the direct fit of the total DFT energies are also shown.

TABLE I: Individual and total intralayer exchange interaction (meV) in both hLFO and hLMO²⁷.

$J_{\alpha,\alpha'(\beta)}$	d_{xy}	$d_{x^2-y^2}$	d_{z^2}	d_{xz}	d_{yz}	J_{MOD}^{ab}	J_{DFT}^{ab}
hLFO	d_{xy}	9.49	3.65	3.20	1.14	0.47	
	$d_{x^2-y^2}$	0.68	9.90	0.88	1.04	0.05	
	d_{z^2}	1.25	5.05	3.58	1.25	0.27	45.2
	d_{xz}	0.56	0.09	0.14	0.01	0.06	
	d_{yz}	0.32	1.00	0.65	0.37	0.06	
hLMO	d_{xy}	10.15	5.81	-0.64	1.17	0.78	
	$d_{x^2-y^2}$	1.28	10.9	-2.71	0.85	0.12	
	d_{z^2}	-	-	-	-	-	29.3
	d_{xz}	0.41	0.17	-0.43	0.01	0.08	
	d_{yz}	0.39	0.85	-0.19	0.31	0.04	

According to the local environment (Fig. 1), the $3d$ orbitals in Fe and Mn are split into $e''(xz, yz)$, $e'(x^2 - y^2, xy)$, and $a_1'(z^2)$ levels by the crystal field, with the increasing energy respectively^{30,31}. It can be seen that the largest SE interactions are contributed by the diagonal hopping processes involving d orbitals of e' symmetry. This is consistent with the physical expectation that SE

is of intralayer nature while d_{xy} and $d_{x^2-y^2}$ are the only d orbitals lying mostly inside the ab plane. Centered on the magnetic ions, these d -like LWFs are also connected with its first neighboring magnetic atoms through the hybridization with the shared oxygen atoms on the bipyramids. As a result, a strong oxygen p character is found on the lobe of the LWFs, pointing to each of the three neighboring oxygen atoms. Considering such d -like LWFs on the hexagonal lattices, a large AFM hopping integral is thus expected along the path of Fe(Mn)-O-Fe(Mn)³². Based on the same orbital symmetry argument, it can be easily seen that the diagonal hopping is relatively smaller for $a_1'(z^2)$ character and almost zero for e'' character. This is because d_{z^2} and $d_{xz}(d_{yz})$ require that the main orbital lobe to be located along z or within the $xz(yz)$ plane which make the hopping integrals much smaller.

Strikingly, the SE interactions also show fundamental difference between the two materials. In hLFO(Fe³⁺:3 d^5 4 s^0), the d_{z^2} orbital of a_1' symmetry is singly occupied and SE interactions can only be of AFM types. However, d_{z^2} is empty in hLMO (Mn³⁺:3 d^4 4 s^0), SE interactions are thus composed of competing AFM and FM types and the coupling strength is further reduced by the forbidden hopping involving the empty d_{z^2} . Thus, a significantly larger AFM coupling energy is observed in hLFO. This is consistent with the higher Néel temperature in hLFO observed in experiment in addition to the larger spin on the Fe site.

Having established the electronic origin of the large intralayer exchange coupling, we now focus on the interlayer exchange coupling $H_{ex}^c = \sum_{i,j,Z_{Fe}} \mathcal{J}_{i,j}^c \vec{S}_i^{Z_{Fe}} \cdot \vec{S}_j^{Z_{Fe}+\frac{c}{2}}$ in hLFO. This is the key to understanding the mechanism of SR and weak FM moment below T_R ⁵. Compared to the SE nature of intralayer exchange, the interlayer Fe ions are coupled by the super super exchange interaction (SSE)³³, in which one Fe atom at $Z_{Fe} = 0$ is in exchange interaction with three first neighbor Fe atoms at $Z_{Fe} = c/2$ mediated by two apical oxygen atoms (O_{ap}). Due to the P6₃cm structure in Fig. 3 (b), the three SSE paths can be further simplified by two independent SSE coupling strengths: J_1^c through Fe₁⁰-O-...-O-Fe₁^c and J_2^c through Fe₁⁰-O-...-O-Fe₂^c respectively. As a result, the H_{ex}^c spin Hamiltonian in Eq. (1) can be rewritten as $H_{ex}^c = \sum_{i,Z_{Fe}} (J_1^c - J_2^c) \vec{S}_i^{Z_{Fe}} \cdot \vec{S}_i^{Z_{Fe}+\frac{c}{2}}$. Obviously, the sign of $\Delta J = J_1^c - J_2^c$ determines the preferred alignment between $\vec{S}_i^{Z_{Fe}}$ and $\vec{S}_i^{Z_{Fe}+\frac{c}{2}}$: parallel (B phase) if $\Delta J < 0$; antiparallel (A phase) if $\Delta J > 0$; no alignment if $\Delta J = 0$, which is the case for P6₃/mmc structure.

Since the non-zero ΔJ comes from the structural distortion (P6₃/mmc \rightarrow P6₃cm), the low temperature spin reorientation must have a structural origin. Here we investigate the dependence of ΔJ on the three phonon modes K_1 , K_3 , and Γ_2^- that are responsible for the structural distortion²⁷. We use DFT to calculate the ΔJ as functions of phonon mode displacements (Q_p , where $p=K_1$, K_3 , and Γ_2^-) and the results are shown in Fig.

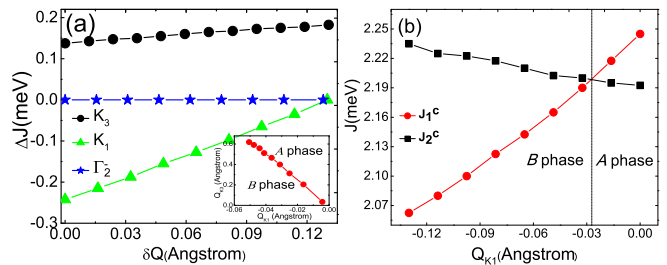


FIG. 3: (Color online.) (a) $\Delta J(\delta Q) = J(Q) - J(Q_0)$ for each individual K_1 , K_3 , and Γ_2^- phonon mode, where $\delta Q = Q - Q_0$ and Q_0 is the value at 300 K, while the other two phonon displacements are kept as zero. Insert: theoretical phase diagram as functions of mode amplitudes of K_1 and K_3 . (b) J_1^c and J_2^c as functions of Q_{K_1} , while Q_{K_3} and $Q_{\Gamma_2^-}$ are fixed at the experimental values²⁷.

3(a). It can be seen that ΔJ depends on the displacement of each phonon mode rather differently.

Clearly, K_1 phonon mode has the largest effect on SR. This can be identified by the steepest slope of ΔJ when K_1 is increased perturbatively, yielding a linear coefficient $\frac{\delta \Delta J}{\delta Q_{K_1}} \sim 1.9 \text{ meV/\AA}$. This suggests a strong tendency of K_1 in driving hLFO from B phase ($\Delta J < 0$) into A phase ($\Delta J > 0$). Indeed this is also consistent with the physical expectation of atomic displacements under the K_1 mode. K_1 phonon is a Brillouin Zone (BZ) boundary mode and is of pure in-plane nature. The atomic displacements of K_1 phonon mostly involve the O_{ap} of FeO₅ (Fig. 1). As shown in Fig. 2(c), the effects of the K_1 are: O_{ap} of Fe₁⁰ moves away from that of Fe₁^c, causing J_1^c to decrease; O_{ap} of Fe₁⁰ moves closer to that of Fe₂^c and Fe₃^c, causing J_2^c to increase. As a result, K_1 is strongly coupled to the ΔJ .

The K_3 phonon mode can be described by the rotation of FeO₅ (Fig. 1(a)) also located at BZ boundary. The atomic displacements of K_3 mode include all the O_{ap} of the FeO₅. However, due to its rotational nature, the atomic displacement of the O_{ap} alternate their directions along c as shown in Fig 2(d). As a result, the overall length of J_1^c and J_2^c paths are barely changed except that the Fe atom is slightly moved away from its equilibrium positions in P6₃/mmc symmetry. Compared with the direct tunability of ΔJ by K_1 mode, the K_3 phonon is expected to be a second order effect in SR. Indeed, our DFT calculation predicts a much weaker variation of ΔJ with increased K_3 phonon mode amplitude, in which the linear coefficient $\frac{\delta \Delta J}{\delta Q_{K_3}} \sim 0.3 \text{ meV/\AA}$ is about one order of magnitude smaller than that of K_1 . Similar to that of K_1 mode, the slope is also positive, favoring the SR from B to A phase.

Finally, we focus on the coupling between Γ_2^- and ΔJ . Γ_2^- is ferroelectric phonon mode at zone center. The atomic displacements of this mode involve all the Lu, O, and Fe atoms moving along c . However, the displacements of the two O_{ap} of one bipyramid are exactly

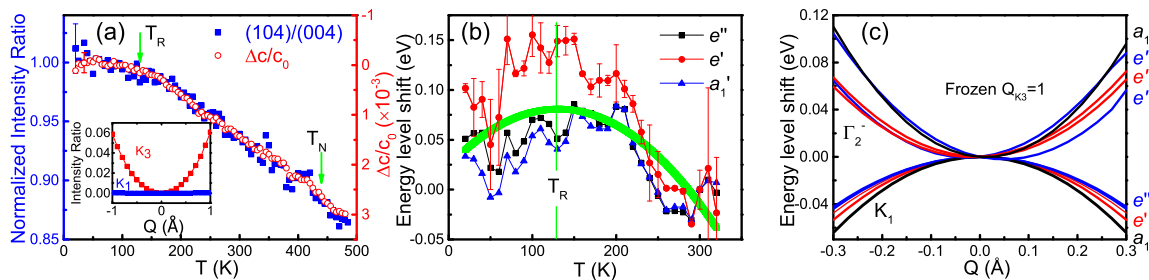


FIG. 4: (Color online.) Structural changes indicated by the XRD and XAS. (a) The XRD intensity ratio between the (104) and (004) peaks (normalized to the 30 K value) and the change of lattice constant c (with respect to the 30 K value) as functions of the temperature (the representative error bars are shown). Inset: the simulated intensity ratio between the (104) and (004) peaks as functions of phonon displacements. (b) The change of Fe-3d crystal field levels (relative to the 300 K values) as functions of the temperature (the error bars for e' levels are shown as examples); the bold line is a guide to the eye to highlight the common peak-like feature. (c) Simulated change of Fe-3d levels as functions of phonon displacements²⁷.

the same. As a result, the SSE paths in J_1^c and J_2^c are changed uniformly. Not surprisingly, our theory predicts a zero dependence of ΔJ on Γ_2^- mode amplitude. It indicates that this ferroelectric distortion alone does not play any role in SR.

The significantly different coupling strengths of ΔJ with the phonon modes suggests the primary role of K_1 phonon mode in SR of hLFO. Indeed, when K_1 mode is frozen into the experimental structural coordinates at $T=300$ K perturbatively, J_1^c and J_2^c rapidly increases and decreases respectively and SR occurs at the crossing point as shown in Fig. 3(b) separating the B from A phase. Below, we show that Q_{K_3} saturates at close to T_R , while Q_{K_1} changes significantly from 300 K to 20 K using XRD and XAS measurements.

As shown in Fig.4(a), the temperature dependence of the normalized intensity ratio between (104) and (004) peaks appears to saturate when temperature is lowered to T_R . We attribute the saturation to the slow variation of K_3 phonon at low temperature, because K_3 is expected to have a dominant effect here, according to the simulated intensity ratio (Fig.4(a) inset)³⁴, while the zone center mode Γ_2 is expected to have no effect. The saturation of K_3 mode can be further confirmed by the temperature dependence of the lattice constant c which follows closely to that of the intensity ratio, as shown in Fig.4(a). The displacement of the K_3 mode includes a rotation of the FeO_5 trigonal bipyramid, which changes the shape of the unit cell by enlarging a and reducing c ⁷; the change of c (Δc) is proportional to ΔQ_{K_3} for small change of Q_{K_3} . The matching temperature dependence in Fig.4(a) suggests that the change of c is indeed caused by the K_3 mode which saturates at low temperature.

XAS measurements suggest that the K_1 mode undergoes a gradual change at low temperature. Previously, we assigned the Fe-3d crystal levels using the XAS at room temperature^{27,30}. As shown in Fig. 4(b), the temperature dependences of the energy levels all show broad peak-like features with the maxima close to T_R . The crystal field levels of Fe-3d are expected to be sensitive

to the shape of FeO_5 . As shown in Fig. 1(a), the K_3 mode causes a rotation of the FeO_5 while the K_1 or Γ_2^- modes cause distortions of the FeO_5 , so the energy-level shift observed in Fig. 4(c) are most likely generated by the change of Q_{K_1} or $Q_{\Gamma_2^-}$. Fig. 4(c) shows a simulation²⁷ of the energy level change of the crystal field levels as functions of Q_{K_1} or $Q_{\Gamma_2^-}$ with respect to the value when all the mode displacements are zero. According to the simulation, the K_1 mode generates a maximum at $Q_{K_1} = 0$ while $Q_{\Gamma_2^-}$ generates a minimum at $Q_{\Gamma_2^-} = 0$; this is because the K_1 mode move both O_{ap} atoms away from the Fe sites and make the FeO_5 larger while the Γ_2^- mode pushes one O_{ap} atom close to Fe site. Comparing the simulation and the observation, we infer that the K_1 mode changes gradually when the temperature is lowered, in order to generate the maximum²⁷; this is consistent with the theoretical prediction in which Q_{K_1} changes when the temperature is lowered and causes the transition from antiferromagnetism in B_2 phase to weak ferromagnetism in A_2 phase.

IV. CONCLUSION

Hence, the roles of all three structural distortions are elucidated in hLFO: the instability of K_3 mode is the driving force of the $P6_3/mmc \rightarrow P6_3cm$ structural transition; the improper ferroelectricity of Γ_2^- mode is induced by frozen K_3 mode^{13,15}; the competing effect between K_1 and K_3 modes determines the magnetic ordering and drives the magnetic phase transition. If the K_1 mode can be tuned by interface engineering³⁵⁻³⁷, the T_R can be increased, achieving the spontaneous electric and magnetic polarizations and their couplings at room temperature.

Acknowledgment

This work is supported by Air Force Office of Scientific Research under award No. FA9550-13-1-0124 (X.Wu).

Computational support is provided by the National Energy Research Scientific Computing Center and by the National Science Foundation through XSEDE resources provided by the XSEDE Science Gateways program (award No. TG-DMR120045). Research supported by the U.S. Department of Energy, Basic Energy Sciences, Materials Sciences and Engineering Division (T.Z.W., X.S.X.). We also acknowledge partial funding support from the National Basic Research Program of China (973 Program) under the grant No. 2011CB921801 (J.S.), the National Natural Science Funds of China Grant No. 11374275 (L.H.) and the US DOE Office of Basic Energy

Sciences, the US DOE grant de-sc0002136 (W.B.W.). Use of the Advanced Photon Source was supported by the U. S. Department of Energy, Office of Science, Office of Basic Energy Sciences, under Contract No. DE-AC02-06CH11357. X. M. Cheng acknowledges support from the National Science Foundation under Grant No. 1053854.

X. Wu is grateful for the useful discussions with Andrei Malashevich, Craig Fennie, Weida Wu, and David Vanderbilt.

* To whom correspondence should be addressed: xifanwu@temple.edu, and xiaoshan.xu@unl.edu.

-
- ¹ M. Stengel, N.A. Spaldin, and D. Vanderbilt, *Nat. Phys.* **5**, 304 (2009).
- ² H. Fu and R. E. Cohen, *Nature* **403**, 281 (2000).
- ³ S. Lee, A. Pirogov, M. Kang, K.-H. Jang, M. Yonemura, T. Kamiyama, S.-W. Cheong, F. Gozzo, N. Shin, H. Kimura, Y. Noda, and J.-G. Park, *Nature* **451**, 805 (2008).
- ⁴ J. H. Lee, *et al. Nature* **466**, 954 (2010).
- ⁵ W. Wang, J. Zhao, W. Wang, Z. Gai, N. Balke, M. Chi, H. N. Lee, W. Tian, L. Zhu, X. Cheng, D. J. Keavney, J. Yi, T. Z. Ward, P. C. Snijders, H. M. Christen, W. Wu, J. Shen, and X. Xu, *Phys. Rev. Lett.* **110**, 237601 (2013).
- ⁶ E. Magome, C. Moriyoshi, Y. Kuroiwa, A. Masuno and H. Inoue, *Jpn. J. Appl. Phys.* **49**, 09ME06 (2010).
- ⁷ A. Muñoz, J. A. Alonso, M. J. Martínez-Lope, M. T. Casáis, J. L. Martínez, and M. T. Fernández-Díaz *Phys. Rev. B* **62**, 9498 (2000).
- ⁸ A. R. Akbashev, A. S. Semisalova, N. S. Perov and A. R. Kaul, *Appl. Phys. Lett.* **99**, 122502 (2011).
- ⁹ I. Dzyaloshinsky, *J. Phys. Chem. Solids* **4**, 241 (1958).
- ¹⁰ T. Moriya, *Phys. Rev.* **120**, 91 (1960).
- ¹¹ A. Malashevich and D. Vanderbilt, *Phys. Rev. Lett.* **101**, 037210 (2008).
- ¹² J. Hong, A. Stroppa, J. Íñiguez, S. Picozzi, and D. Vanderbilt, *Phys. Rev. B* **85**, 054417 (2012).
- ¹³ H. Das, A. L. Wysocki, Y. Geng, W. Wu and Craig J. Fennie, *Nat. Commun.*, **5**, 2998 (2014).
- ¹⁴ Y. Geng, H. Das, A. L. Wysocki, X. Wang, S. -W. Cheong, M. Mostovoy, C. J. Fennie and W. Wu, *Nature Mater.*, **10**, 3813 (2013).
- ¹⁵ C. J. Fennie and K. M. Rabe *Phys. Rev. B* **72**, 100103 (2005).
- ¹⁶ N. A. Spaldin, S. -W. Cheong, R. Ramesh, *Phys. Today* **63**, 38 (2010).
- ¹⁷ J. Wang, *et al. Science* **299** 1719 (2003).
- ¹⁸ J. B. Neaton, C. Ederer, U. V. Waghmare, N. A. Spaldin, and K. M. Rabe, *et al. Phys. Rev. B* **71** 014113 (2005).
- ¹⁹ T. Lancaster, *Phys. Rev. Lett.* **98**, 197203 (2007).
- ²⁰ X. Fabrèges, S. Petit, I. Mirebeau, S. Pailhès, L. Pinsard, A. Forget, M. T. Fernandez-Diaz, and F. Porcher, *Phys. Rev. Lett.* **103**, 067204 (2009).
- ²¹ P. J. Brown and T. Chatterji, *J. Phys. Condens. Matter* **18**, 10085 (2006).
- ²² K. I. Kugel and D. I. Khomskii, *Sov. Phys. Usp.* **25**, 231 (1982).
- ²³ N. Marzari, A. A. Mostofi, J. R. Yates, I. Souza, and D. Vanderbilt, *et al.*, *Rev. Mod. Phys.* **84**, 1419 (2012).
- ²⁴ P. H.-L. Sit, Roberto Car, Morrel H. Cohen, and A. Selloni, *Inorg. Chem.* **50**, 10259 (2011).
- ²⁵ I. V. Solovyev, M. V. Valentyuk, and V. V. Mazurenko, *Phys. Rev. B* **86**, 054407 (2012).
- ²⁶ I. V. Solovyev, *J. Phys: Condens. Matter* **20**, 293201(2008).
- ²⁷ See Supplemental Material at <http://link.aps.org/supplemental/> for more detailed information on the theoretical model and calculation, phonon mode decomposition, analysis of the x-ray absorption spectra, and simulation of crystal field levels.
- ²⁸ G. Kresse, and J. Furthmüller, *Phys. Rev. B*, **54**, 11169 (1996).
- ²⁹ H. J. Xiang, E. J. Kan, S. -H. Wei, M. -H. Whangbo, and X. G. Gong, *Phys. Rev. B* **84**, 224429 (2011).
- ³⁰ W. Wang, H. Wang, X. Xu, L. Zhu, L. He, E. Wills, X. Cheng, D. J. Keavney, J. Shen, X. Wu, X. Xu, *Appl. Phys. Lett.* **101**,241907 (2012).
- ³¹ D.-Y. Cho, J. -Y. Kim, B.-G. Park, K.-J. Rho, J. -H. Park, H. -J. Noh, B. J. Kim, S. -J. Oh, H. -M. Park, J. -S. Ahn, H. Ishibashi, S.-W. Cheong, J. H. Lee, P. Murugavel, T. W. Noh, A. Tanaka, and T. Jo, *Phys. Rev. Lett.* **98**, 217601 (2007).
- ³² P. W. Anderson, *Phys. Rev.* **79**, 350 (1950).
- ³³ M.-H. Whangbo, H.-J. Koo, D. Dai, *J. Solid. State. Chem.*, **176** 417 (2003).
- ³⁴ B. D. Cullity, *Elements of X-Ray Diffraction.* (Addison-Wesley Pub. Co., Reading, Mass., 1956).
- ³⁵ J. H. Lee, and K. M. Rabe, *Phys. Rev. Lett.* **104**, 207204 (2010).
- ³⁶ O. Diéguez, K.M. Rabe, and D. Vanderbilt, *Phys. Rev. B* **72**, 144101 (2005).
- ³⁷ J. Junquera, and P. Ghosez, *Nature* **422**, 506 (2003).